PNAS RESEARCH ARTICLE | MEDICAL SCIENCES

Fluorinated lipid nanoparticles enable real-time tracking of mRNA delivery and uncover spatiotemporal mechanisms of immune activation

Kairu Xie[a,1], Lijun Zhu[a,b,1], Mojie Duan[a], Yu Fu[a,b], Haiqiang Wang[a,b], Yuhan Shen[a,c], Yu Li[a,b], Ruifang Wang[a,b], Zhong-Xing Jiang[a,b], Shizhen Chen[a,b,c], Jung Soo Suk[d], Daiqin Chen[a,b,2], and Xin Zhou[a,b,c,2]

Affiliations are included on p. 10.

Edited by Catherine Murphy, University of Illinois at Urbana-Champaign, Urbana, IL; received July 25, 2025; accepted December 2, 2025

Messenger RNA (mRNA) vaccines rely on lipid nanoparticles (LNPs) for in vivo delivery, yet conventional formulations exhibit inefficient tissue targeting, undesired hepatic accumulation, and limited understanding of the delivery–response relationship, constraining their therapeutic precision and safety. Here, we report the development of fluorinated LNPs (FLNPs) that enable real-time tracking of mRNA biodistribution and expression via ^{19}F magnetic resonance spectroscopy/imaging (NMR/MRI)" rather than "magnetic resonance spectroscopy/MRI (NMR). These FLNPs retain robust protein expression comparable to clinical LNPs, while reducing liver accumulation by 94.6%. By integrating fluorine signal quantification with spatial analysis of mRNA translation and antigen presentation, we establish a direct correlation between carrier localization, antigen expression kinetics, and immune cell trafficking. Specifically, we show that antigen-presenting cells internalize FLNP-mRNA at the injection site and subsequently migrate to draining lymph nodes, enabling localized immune priming with minimal systemic exposure. This work provides mechanistic evidence linking in vivo nanocarrier trafficking with spatiotemporal immune activation, offering insights into how delivery kinetics govern vaccine efficacy. The FLNP platform thus enables both precision mRNA delivery and noninvasive tracking, representing a powerful tool for mechanistic studies and rational design of next-generation mRNA vaccines.

^{19}F magnetic resonance spectroscopy | lipid nanoparticles | fluorination | mRNA vaccine | nucleic acid delivery

Significance

We demonstrate a fluorinated lipid nanoparticle (FLNP) system that not only delivers nucleic acids efficiently but also enables noninvasive real-time tracking of biodistribution and expression using ^{19}F NMR/MRI. This dual functionality provides a mechanistic link between nanocarrier trafficking, antigen expression kinetics, and immune cell migration in vivo. By reducing undesired hepatic accumulation and revealing that antigen-presenting cells at the injection site initiate localized immune priming before trafficking to draining lymph nodes, FLNPs address long-standing challenges in precision vaccine delivery. These findings highlight FLNPs as a transformative platform for both basic mechanistic studies and the rational design of next-generation messenger RNA (mRNA) vaccines with enhanced safety, precision, and monitoring capability.

Messenger RNA (mRNA) therapeutics, particularly mRNA vaccines, have emerged as a transformative modality for infectious disease prevention and cancer immunotherapy (1–3). Lipid nanoparticles (LNPs) have become the leading platform for mRNA delivery due to their efficient encapsulation, protection of nucleic acids, and facilitation of cytosolic release (4). Despite this success, conventional LNPs exhibit several limitations, including preferential hepatic accumulation, suboptimal transfection efficiency in target tissues, and lack of real-time information regarding their in vivo fate (5–7). These limitations not only restrict tissue-specific therapeutic applications but also hinder mechanistic understanding of the spatiotemporal interplay between mRNA delivery, expression, and immune activation (8).

To illuminate these limitations, it is instructive to compare mRNA-LNPs with traditional subunit vaccines. While subunit vaccines rely on well-defined mechanisms of antigen transport to lymph nodes (LNs) via passive drainage or uptake by antigen-presenting cells (APCs), the biodistribution and cellular processing of mRNA-LNP vaccines remain poorly understood (9, 10). Following intramuscular administration, three potential pathways may contribute to immune activation: 1) local expression of mRNA-encoded antigens, followed by immune cell recruitment; 2) APC uptake and migration to LNs; or 3) direct LNP drainage to LNs (11–13). Although all routes can prime adaptive immunity, the relative contributions and spatiotemporal dynamics of these routes remain unclear (14, 15). Moreover, existing delivery systems lack quantitative, noninvasive tools to track these processes in real time, hindering rational optimization of LNP formulations.

Recent advances in fluorination chemistry offer promising solutions to these challenges. Specifically, the strategic incorporation of fluorinated lipids in LNPs improves serum stability, enhances cellular uptake, and promotes endosomal escape of nucleic acid cargos while reducing toxicity related to delivery materials (16–18). Building on these advantages, we developed a fluorinated LNP (FLNP) platform featuring fluorinated analogs of conventional ionizable lipids that maintain nucleic acid binding capacity. Our optimized FLNPs demonstrate superior performance characteristics, including enhanced cellular

Author contributions: K.X., D.C., and X.Z. designed research; K.X., L.Z., M.D., Y.F., H.W., Y.S., Y.L., and R.W. performed research; L.Z. and Y.L. contributed new reagents/analytic tools; K.X., L.Z., Y.L., Z.-X.J., S.C., and D.C. analyzed data; and K.X., Z.-X.J., J.S.S., D.C., and X.Z. wrote the paper.

The authors declare no competing interest.

This article is a PNAS Direct Submission.

[1]K.X. and L.Z. contributed equally to this work.

[2]To whom correspondence may be addressed. Email: chendychin@apm.ac.cn or xinzhou@wipm.ac.cn.

This article contains supporting information online at https://www.pnas.org/lookup/suppl/doi:10.1073/pnas.2519823123/-/DCSupplemental.

Published January 2, 2026.

internalization, more efficient endosomal escape, and mitigating nonproductive leakage during endocytosis, leading to more efficient intracellular release and protein expression.

Beyond improved delivery properties, the inclusion of fluorinated components enables real-time tracking through ^{19}F magnetic resonance techniques (NMR/MRI) (19). It offers distinct advantages for noninvasive tracking, including high specificity due to negligible endogenous background and quantitative signal correlation with probe concentration (20). However, its application to lipid-based mRNA nanocarriers remains largely unexplored (21). To address this gap, we engineered FLNPs with distinct ^{19}F signatures, enabling monitoring of carrier biodistribution in vivo. Intriguingly, we observed that ^{19}F NMR signals from FLNPs exhibit reversible suppression and recovery, reflecting dynamic nucleic acid binding and release. These signal fluctuations correlate with antigen expression, offering a real-time readout of delivery kinetics and vaccine efficacy.

In this study, we engineered a panel of FLNPs with tunable fluorinated lipid content and employed ^{19}F NMR to monitor their delivery performance in real time. We validated this strategy in vivo and demonstrated that optimized FLNPs achieve robust protein expression at the injection site with significantly reduced liver accumulation by 94.6%. Combining ^{19}F NMR with qPCR further allowed us to delineate antigen trafficking from local expression to LN engagement, shedding light on the underlying mechanisms of immune activation.

Taken together, our findings establish a powerful, noninvasive platform for the rational design and real-time optimization of next-generation mRNA vaccines. FLNPs not only mitigate key delivery bottlenecks but also enable dynamic performance evaluation, offering substantial value for translational mRNA-LNP applications.

Results

Design and Synthesis of Fluorinated Lipids. To assess whether the incorporation of fluorinated lipids into LNPs could enhance nucleic acid transfection efficiency, we synthesized two lipids: bis(12-(perfluoro-*tert*-butoxyl)dodecyl)amine (FC12) and bis(6-(perfluoro-*tert*-butoxyl)hexyl)amine (FC6). Both lipids bear a secondary amine and two symmetrical long alkyl chains. Under physiological pH, the secondary amine becomes protonated, enabling effective electrostatic interaction with negatively charged nucleic acids. The single alkyl chain contains 12 carbon atoms in FC12 and 6 carbon atoms in FC6, respectively. In addition, the presence of two perfluoro-*tert*-butyl groups provides a strong and well-resolved fluorine signal, facilitating sensitive tracking of lipid-nucleic acid interactions by fluorine magnetic resonance techniques (Fig. 1*A*). The chemical structure of FC12 and FC6 was confirmed by ^{1}H, ^{13}C, and ^{19}F NMR spectroscopy, and high-resolution mass spectrometry (HRMS).

Comprehensive Physicochemical Assessment and ^{19}F NMR Analysis of FLNPs. To assess whether incorporating fluorinated lipids into LNPs affects their physicochemical characteristics and ^{19}F NMR properties, we formulated a series of LNPs. The control formulation was based on the composition used in Moderna's COVID-19 vaccine, consisting of SM102, DSPC, cholesterol, and DMG-PEG2000 at a molar ratio of 50:10:38.5:1.5 (22). For the experimental group, 50% of SM102 was replaced with either FC6 or FC12, yielding a molar ratio of 25:25:10:38.5:1.5 for the fluorinated lipid, SM102, DSPC, cholesterol, and DMG-PEG2000, respectively. Plasmid DNA (pDNA) was selected as the model cargo, owing to its larger molecular weight, which can induce prominent alterations in ^{19}F NMR signals upon interaction with fluorinated lipids (23, 24). The lipids and pDNA were mixed at a 1:3 volume ratio to form the conventional LNPs (LNP-SM102) and FLNPs (LNP-25%FC12 and LNP-25%FC6) (Fig. 1*B*).

The physicochemical properties of the resulting LNPs were characterized. Cryogenic electron microscopy (Cryo-EM) showed that all LNPs formed dense, spherical particles with a multilamellar shell surrounding an amorphous core (Fig. 1*C*), and had an average diameter of approximately 100 nm. Dynamic light scattering (DLS) measurements indicated hydrodynamic diameters of 107 ± 7 nm for LNP-SM102, 117 ± 5 nm for LNP-25%FC12, and 101 ± 4 nm for LNP-25%FC6, with corresponding polydispersity indices (PDIs) of 0.141 ± 0.014, 0.194 ± 0.003, and 0.144 ± 0.003, respectively (Fig. 1*D*). These results suggest that the incorporation of fluorinated lipids did not significantly alter LNP morphology, size, or size distribution.

Encapsulation efficiency was quantified by labeling pDNA with Cy5 and measuring fluorescence intensity against a calibration curve. The efficiencies were 80.0 ± 3.4% for LNP-SM102, 82.5 ± 2.4% for LNP-25%FC12, and 79.8 ± 3.9% for LNP-25%FC6, indicating effective loading across all formulations (*SI Appendix*, Table S1).

To assess protection against nuclease degradation, LNPs were treated with DNase I and analyzed by agarose gel electrophoresis. Heparin was employed to disrupt LNP integrity, exposing encapsulated nucleic acids to degradation. All three formulations effectively protected nucleic acids from DNase I degradation (Fig. 1*E* and *SI Appendix*, Fig. S1). Notably, the nucleic acids remained intact even after exposure to a compression nebulizer followed by DNase I treatment, underscoring the potential of FLNPs for pulmonary gene delivery (*SI Appendix*, Fig. S2).

^{19}F NMR was employed to confirm the integration of fluorinated lipids into LNPs. A marked attenuation of the ^{19}F signal, measured relative to a CF_3NaO_3S reference solution (–79.6 ppm), was observed in both FC12- and FC6-containing formulations (Fig. 1*F*). This reduction is likely due to the restricted mobility of fluorine atoms caused by their interaction with nucleic acids within the LNP. This hypothesis was further supported by longitudinal (T_1) and transverse (T_2) relaxation time measurements: Both T_1 and T_2 were significantly reduced in FLNPs compared to free fluorinated lipids (*SI Appendix*, Table S2), indicating diminished molecular motion (25, 26).

To validate this mechanism, methanol was used to disrupt the LNP structures. This treatment liberated the fluorinated lipids, restoring fluorine mobility and partially recovering the ^{19}F NMR signal (Fig. 1*G*). Collectively, these findings confirm the successful incorporation of fluorinated lipids into LNPs and demonstrate that fluorine signal attenuation arises from constrained mobility within the LNP architecture.

Screening of the Optimal FLNP Formulation for In Vitro Nucleic Acid Delivery. To assess whether FLNPs enhance nucleic acid delivery, we transfected 293T cells using LNPs (0.195 ng/μL) encapsulating plasmids for enhanced green fluorescent protein (pEGFP) or luciferase (pLuc). The physicochemical properties of these formulations were characterized (*SI Appendix*, Fig. S3 and Table S1). Cell viability remained above 80% across all treatment groups, indicating negligible cytotoxicity (*SI Appendix*, Fig. S4).

Among the tested LNPs, LNP-25%FC12 significantly outperformed both LNP-SM102 and LNP-25%FC6 in transfection efficiency. Confocal laser scanning microscopy (CLSM) revealed more extensive EGFP expression in cells treated with LNP-25%FC12 compared to LNP-SM102. Quantitative analysis using Image J demonstrated a 7.1-fold increase in EGFP fluorescence in the LNP-25%FC12 group relative to the control (Fig. 2 *A* and *B*).

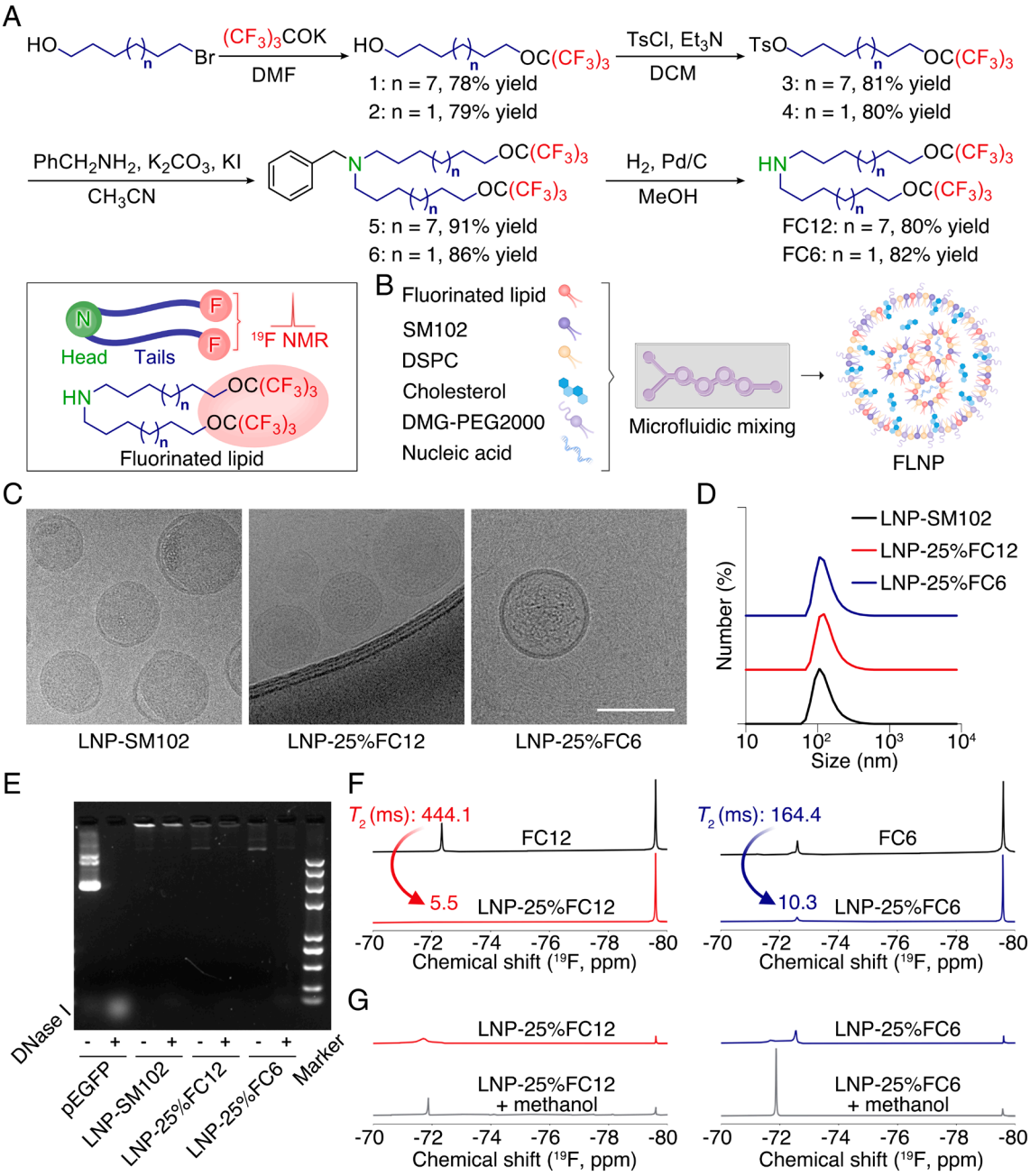

Fig. 1. Characterization of FLNPs. (*A*) The synthesis of FC12 and FC6. Illustration showing the secondary amine headgroup, alkyl chains (tails), and perfluoro-*tert*-butyl groups that provide a single and well-resolved fluorine signal. (*B*) Schematic illustrating the formulation of FLNP. (*C*) Representative cryo-TEM images of LNPs. (Scale bar, 100 nm.) (*D*) Hydrodynamic size distribution of LNPs determined by DLS. A representative result is shown. (*E*) Agarose gel retardation assays of LNPs with or without DNase I treatment, free pEGFP served as a control. (*F*) ^{19}F NMR of fluorinated Lipids and FLNPs. (*G*) ^{19}F NMR of FLNPs with or without methanol treatment. CF_3NaO_3S (−79.6 ppm) was used as the ^{19}F NMR reference at 128.7 mM (*F*) and 1 mM (*G*). pEGFP: Plasmid DNA encoding EGFP.

Similarly, luciferase activity quantified by luminescence assay showed a 6.8-fold enhancement in the LNP-25%FC12 group compared to LNP-SM102 (Fig. 2*C*).

To investigate the molecular mechanisms by which FC12 and FC6 influence LNP transfection efficiency, we constructed LNP lipid bilayers and characterized their structural properties through long-time all-atom molecular dynamics simulations. Our results show that FC12 significantly enhances the rigidity of the lipid membrane. Specifically, compared to the SM102 system, incorporation of 25% FC12 increased the overall lipid order parameter while reducing the average lipid area (*SI Appendix*, Fig. S5 *A* and *B*). In contrast, due to its shorter tail length, FC6 led to a more disordered lipid arrangement, with a decreased tail order parameter and an increased average lipid area. This looser packing facilitated water penetration into the bilayer (*SI Appendix*, Fig. S5*C*), thereby compromising membrane stability and potentially LNP integrity. Furthermore, the results also indicate that FC12 has a certain impact on lipid fluidity; the bilayer containing 25% FC12 exhibited markedly higher fluidity than the other systems (*SI Appendix*, Fig. S5*D*). These findings suggest that FC12 enhances both the stability and fluidity of the LNP membrane, which may underlie its role in improving the DNA transfection efficiency.

To determine the optimal fluorinated lipid content, we synthesized LNPs with varying FC12-to-SM102 molar ratios: LNP-12.5%FC12 (3:1), LNP-25%FC12 (1:1), and LNP-37.5%FC12 (1:3). All formulations exhibited comparable size, PDI, and ζ-potential (Fig. 2*D*) and

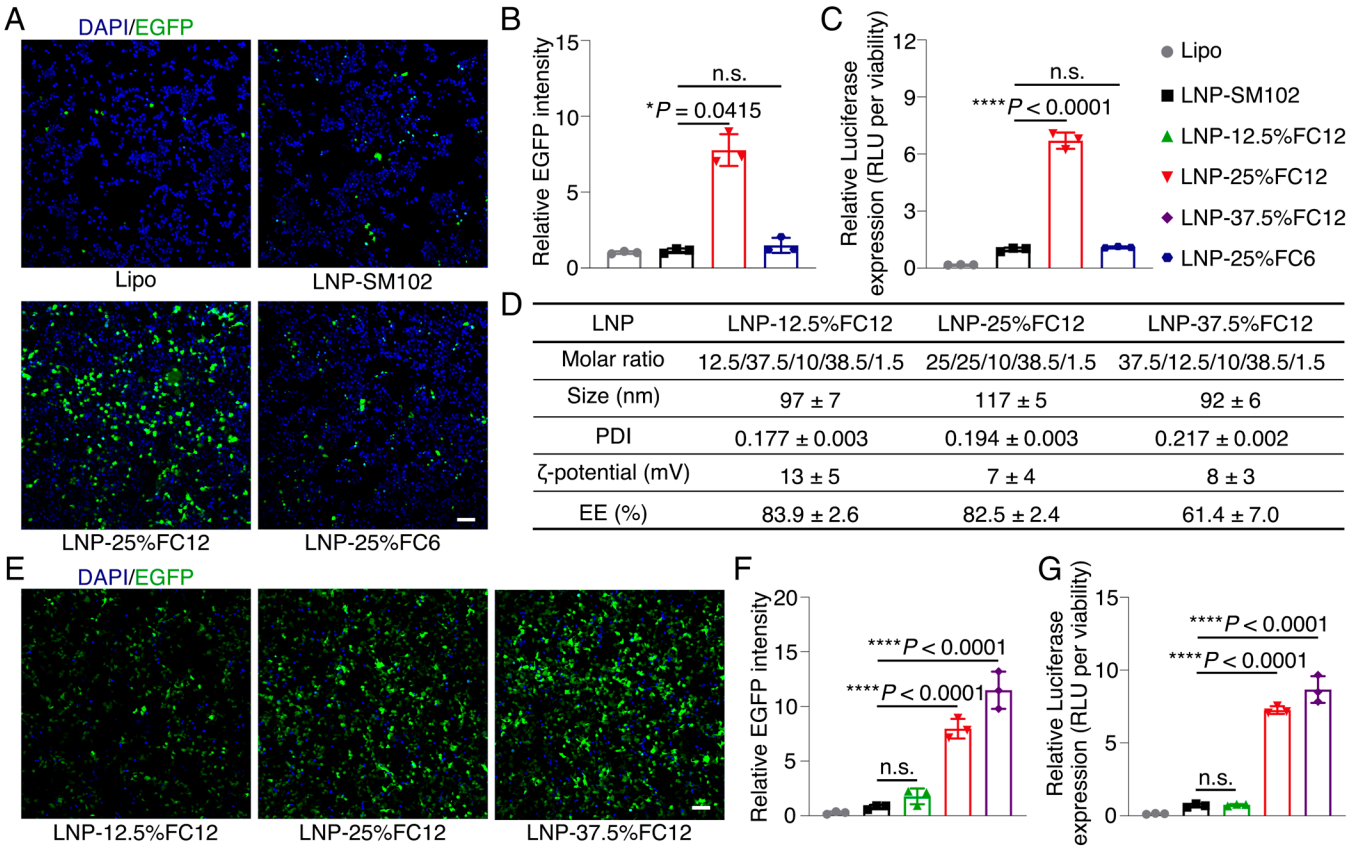

LNP	LNP-12.5%FC12	LNP-25%FC12	LNP-37.5%FC12
Molar ratio	12.5/37.5/10/38.5/1.5	25/25/10/38.5/1.5	37.5/12.5/10/38.5/1.5
Size (nm)	97 ± 7	117 ± 5	92 ± 6
PDI	0.177 ± 0.003	0.194 ± 0.003	0.217 ± 0.002
ζ-potential (mV)	13 ± 5	7 ± 4	8 ± 3
EE (%)	83.9 ± 2.6	82.5 ± 2.4	61.4 ± 7.0

Fig. 2. Screening of the optimal FLNP formulation. (*A*) Representative fluorescent images of EGFP expression in 293T cells following treatment with pEGFP-loaded LNPs. The commercial transfection reagent Lipo8000 (Lipo) was used as a control. (Scale bar, 100 μm.) (*B*) LNP-mediated pEGFP delivery (n = 3). 293T cells were treated with pEGFP-loaded LNP (390 ng) or free pEGFP (390 ng per well) for 48 h. (*C*) LNP-mediated pLuc delivery (n = 3). 293T cells were treated with pLuc-loaded LNP (40 ng) or free pLuc (40 ng per well) for 48 h. (*D*) Physicochemical properties of LNP-FC12 formulations (n = 3). The molar ratio of lipid components is shown: FC12/SM102/DSPC/cholesterol/DMG-PEG2000. (*E*) Representative fluorescent images of EGFP expression in 293T cells following treatment with LNPs for 48 h. (Scale bar, 100 μm.) (*F*) LNP-mediated pEGFP delivery (n = 3), same conditions as in (*B*). (*G*) LNP-mediated pLuc delivery (n = 3), same conditions as in (*C*). pLuc: Plasmid DNA encoding firefly luciferase.

maintained cell viability above 80% at pDNA concentrations below 0.5 ng/μL (*SI Appendix*, Fig. S4).

Transfection efficiency was assessed using both pEGFP and pLuc reporters. All FLNPs exhibited higher gene expression levels than the benchmark LNP-SM102, and transfection efficacy positively correlated with the proportion of FC12 (Fig. 2 *E*–*G*). Notably, LNP-37.5%FC12 yielded 14.4-fold and 12.3-fold increases in EGFP and luciferase expression, respectively, compared to LNP-SM102. However, LNP-37.5%FC12 displayed a considerably lower nucleic acid encapsulation efficiency (61.4 ± 7.0%) compared to the other formulations (Fig. 2*D*). We studied the DNA-binding abilities of FC12 and SM102 molecules using the molecular docking method. The results show that the head groups of both FC12 and SM102 can insert into the minor groove of DNA, forming several stable polar interactions. Compared with FC12, SM102 has lower binding energy and stronger binding ability with DNA (–3.947 kcal/mol for FC12 and –4.535 kcal/mol for SM102) (*SI Appendix*, Fig. S6). The results indicate that SM102 has greater DNA adhesion ability, thereby enabling stronger encapsulation ability of LNP.

Balancing protein expression with encapsulation performance, LNP-25%FC12 emerged as the most practical and cost-effective option for further studies. It achieved a 7.1-, and 6.8-fold increase in EGFP and luciferase expression relative to LNP-SM102, respectively; while maintaining a high encapsulation efficiency of 82.5 ± 2.4%.

Mechanistic Exploration of Enhanced Nucleic Acid Transfection by FLNPs. The efficient intracellular release of nucleic acids is a critical determinant of transfection efficiency. To elucidate the interaction between ionizable lipids and nucleic acids within LNPs, we fluorescently labeled SM102 and FC12 with Cy3 and the pEGFP plasmid with Cy5. These labeled components were used to formulate corresponding LNPs (*SI Appendix*, Fig. S7). Fluorescence spectroscopy confirmed the occurrence of Förster resonance energy transfer (FRET), demonstrating electrostatic interactions between the ionizable lipids (SM102 or FC12) and pEGFP (*SI Appendix*, Fig. S8). Loss of FRET signal upon nucleic acid release confirmed the lipid-DNA dissociation (Fig. 3*A*).

To investigate intracellular trafficking, CLSM was performed 2 h postincubation to capture early endocytosis events. Cells treated with LNP-25%FC12 displayed significantly stronger red fluorescence (Cy5, marked by white arrows) compared to those treated with LNP-SM102, indicating substantially lower exposure of pEGFP during endocytosis and higher cell uptake (Fig. 3*B*). Given that even the transient leakage of nucleic acid cargoes can lead to degradation by DNase I, the improved protection of pEGFP within LNP-25%FC12 likely contributes to its higher transfection efficacy compared to LNP-SM102 (Fig. 3*C*).

To quantify cellular uptake, we employed CLSM and flow cytometry using Cy5-labeled pEGFP. CLSM revealed remarkably stronger fluorescence (marked by white arrows) in cells incubated

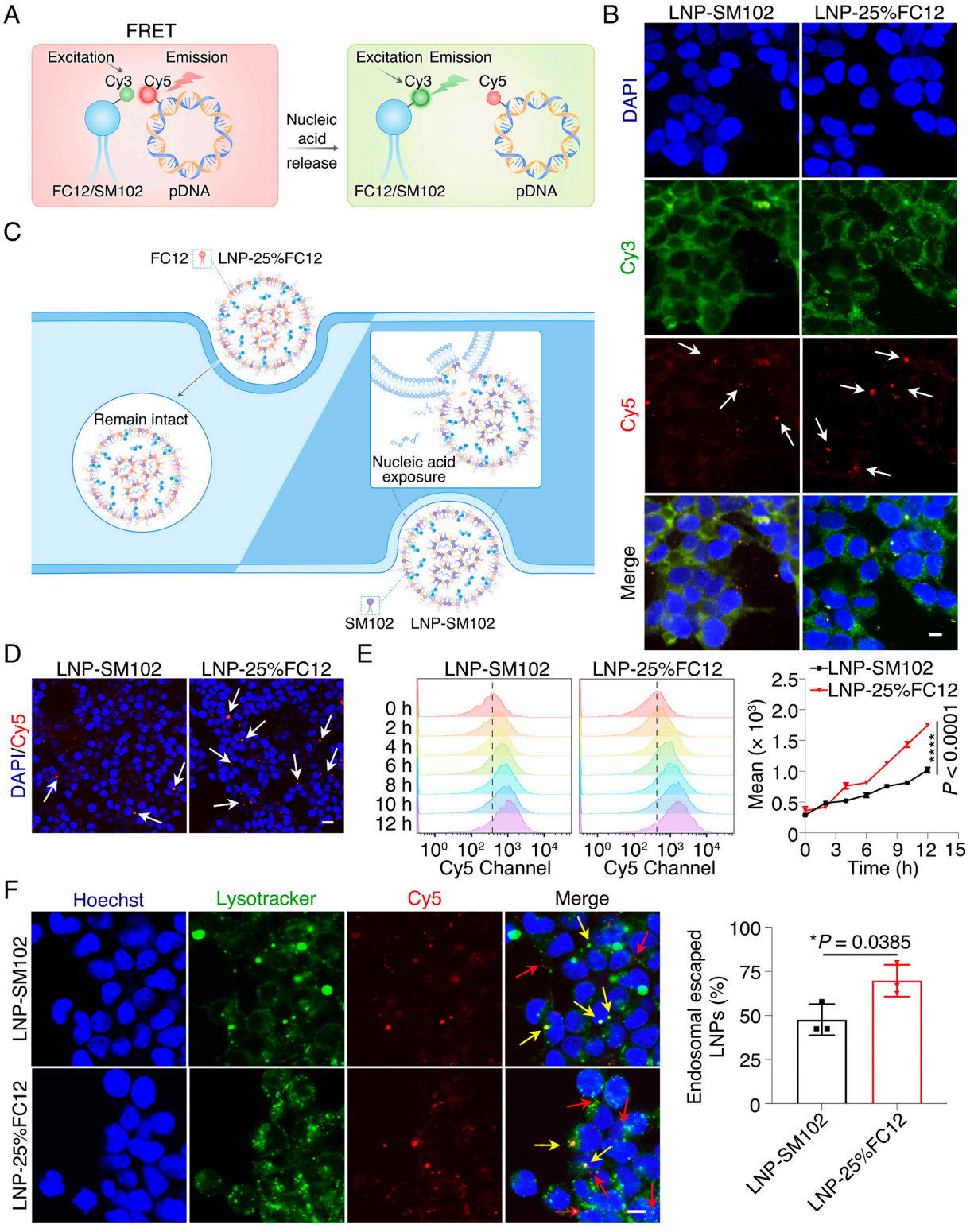

Fig. 3. Mechanistic exploration of enhanced nucleic acid transfection by FLNPs. (*A*) Scheme illustration of the FRET-based method for assessing nucleic acid release. (*B*) Representative confocal images of 293T cells treated with Cy3- and Cy5-labeled LNPs for 2 h; nuclei stained with DAPI (blue). (Scale bar. 10 μm.) (*C*) Schematic representation of the proposed hypothesis that FLNPs reduce nucleic acid exposure during endocytosis. (*D*) Representative confocal images of Cy5-labeled LNP uptake in 293T cells after 12 h; nuclei stained with DAPI (blue). (Scale bar, 20 μm.) (*E*) Flow cytometry of 293T cells treated with Cy5-labeled LNPs over 0 to 12 h (n = 3). (*F*) Representative confocal images showing LNP endosomal escape in 293T cells treated with Cy5-labeled LNPs for 4 h, stained with LysoTracker Green and Hoechst 33342. Endosomal escape efficiency was quantified using ImageJ by calculating the ratio of the red signal in the merged image (escaped LNPs) to the Cy5 image (internalized LNPs) (n = 3). (Scale bar, 10 μm.)

with LNP-25%FC12 than with LNP-SM102 (Fig. 3*D* and *SI Appendix*, Fig. S9). Consistent with these observations, flow cytometry revealed that LNP-25%FC12 achieved 1.5-fold higher uptake than LNP-SM102 at 4 h and 1.7-fold higher uptake at 12 h (Fig. 3*E*). These results indicate that enhanced cellular uptake is a key contributor to the improved transfection efficiency.

Additionally, endosomal escape, a critical step to ensure nucleic acid delivery, was assessed using CLSM. At 2 h and 4 h postincubation,

cells treated with LNP-25%FC12 exhibited notably stronger red fluorescence (marked by red arrows) than those treated with LNP-SM102, indicating enhanced endosomal escape (Fig. 3*F* and *SI Appendix*, Fig. S10). In contrast, cells treated with LNP-SM102 showed more colocalized yellow signals (marked by yellow arrows), signifying endosomal entrapment. Quantitative analysis using Image J revealed that the endosomal escape efficiency of LNP-25%FC12 was approximately 1.5-fold higher than that of LNP-SM102 (Fig. 3*F*).

Correlation between ^{19}F NMR Signal Recovery and Nucleic Acid Release during FLNP Transfection. To investigate the relationship between fluorine signal recovery and nucleic acid release, we monitored the ^{19}F NMR signals of 293T cells treated with LNP-25%FC12 over a time course from 6 to 48 h. A time-dependent increase in ^{19}F signal recovery was observed, plateauing at approximately 18 h (Fig. 4 *A* and *B*). These findings suggest that ^{19}F signal recovery precedes maximal protein expression, which typically requires 48 h, and may serve as an early indicator of LNP disassembly and nucleic acid release.

We then measured the ^{19}F NMR signals in 293T cells treated with LNPs containing varying ratios of FC12 (12.5%, 25%, 37.5%) (Fig. 4*C*). The recovered ^{19}F NMR signal intensity was positively correlated with reporter gene expression, with a linear correlation coefficient of 0.9629 (Fig. 4*D*). The observed ^{19}F NMR signal changes were consistent with the ^{19}F MRI signal intensities from cell lysate treated with LNP-25%FC12 for 48 h (Fig. 4*E*). In addition, cells treated with LNP-25%FC6 also showed partial restoration of the ^{19}F NMR signal, although the signal magnitude was markedly lower than that of the LNP-25%FC12 group, suggesting less extensive lipid and nucleic acid release and correspondingly reduced transfection efficiency (*SI Appendix*, Fig. S11).

These results support a mechanistic model wherein FLNPs, following the endosomal escape, disassemble to release fluorinated lipids and nucleic acids. This release facilitates both protein expression and restoration of the fluorine signal by altering the microenvironment and molecular dynamics of the fluorinated lipids, thereby increasing ^{19}F NMR detectability. Accordingly, ^{19}F signal recovery reflects the extent of nanoparticle disassembly and nucleic acid release, serving as a surrogate marker for transfection efficiency (Fig. 4*F*).

To validate this correlation in vivo, we administered LNP-37.5%FC12 and LNP-25%FC6 into both sides of the gastrocnemius muscle of mice and acquired ^{19}F NMR data 48 h postinjection. The LNP-37.5%FC12 group showed greater restoration of the target peak signal compared to LNP-25%FC6 (Fig. 4*G* and *SI Appendix*, Fig. S12), consistent with the lysate NMR results (*SI Appendix*, Fig. S13). Moreover, ^{19}F MRI revealed a visible signal at the injection site for the LNP-37.5%FC12 group, further corroborating the in vivo disassembly and signal recovery (Fig. 4*H*).

Postmortem analysis of cryosectioned gastrocnemius tissues revealed stronger EGFP fluorescence in the LNP-37.5%FC12 group compared to the LNP-25%FC6 group (*SI Appendix*, Fig. S14). In a separate cohort, mice were injected with LNPs encapsulating luciferase mRNA (mLuc), and bioluminescence imaging showed significantly stronger signal-5.8-fold higher-in the LNP-37.5%FC12 group than in the LNP-25%FC6 group (Fig. 4*I*). Hematoxylin and eosin (H&E) staining confirmed the absence of local tissue damage or inflammatory response following LNP administration (*SI Appendix*, Fig. S14).

Collectively, these results establish a quantitative correlation between ^{19}F NMR/MRI signal recovery and FLNP disassembly in vivo, thereby enabling noninvasive monitoring of nucleic acid release and subsequent protein expression.

In Vivo mRNA Transfection by FLNPs and Colocalization of Expressed Protein and Immune Cells in dLNs. To explore the potential of FLNPs for mRNA delivery in nucleic acid vaccines, we synthesized and characterized mRNA-loaded LNP-SM102 and FLNPs, assessing their transfection efficiency both in vitro and in vivo (*SI Appendix*, Fig. S3 and Table S3). In vitro, FLNPs exhibited slightly reduced mRNA transfection efficiency compared to LNP-SM102 (*SI Appendix*, Figs. S15 and S16). However, in vivo bioluminescence imaging revealed that LNP-25%FC12 achieved comparable transfection efficiency to LNP-SM102 while markedly attenuating liver expression (Fig. 5 *A–C* and *SI Appendix*, Fig. S17). This reduced off-target expression observed with FLNPs suggests a lower risk of hepatotoxicity, an advantageous property for mRNA vaccine delivery.

To further evaluate the vaccine delivery potential of FLNPs, we administered mLuc-loaded LNP-SM102 or LNP-25%FC12 via subcutaneous (s.c.) injection at the tail base of BALB/c nude mice. Luciferase expression was imaged 24 h postinjection using in vivo bioluminescence (Fig. 5*D*). Consistent with results from intramuscular injections, LNP-25%FC12-treated mice displayed lower hepatic luciferase expression. Both LNP formulations primarily transfected the injection site and reached the inguinal lymph nodes (iLNs), with comparable transfection efficiency at both locations (Fig. 5 *E* and *F*). These results indicate that FLNPs can localize antigen expression to both injection and lymphoid sites while minimizing systemic exposure.

To further investigate FLNP biodistribution, we performed ^{19}F NMR on tissue lysates from iLNs and tail base of FLNP-treated mice. A detectable ^{19}F signal was observed only at the injection site, indicating localized disassembly of FLNPs (Fig. 5*G*). Protein expression, however, was observed in both the injection site and iLNs. Quantitative PCR analysis of EGFP mRNA revealed that the majority of the delivered mRNA remained at the injection site, with only trace amounts detected in the iLNs (Fig. 5*H*). These results suggest that while FLNPs predominantly degrade locally, the expressed protein products—rather than the LNPs or mRNA—are transported to the draining lymph nodes.

To investigate the cellular mechanisms underlying this transport, we performed CLSM on cryosectioned iLN. EGFP signal was found to colocalize with CD169, a surface marker of subcapsular sinus macrophages and specialized antigen-presenting cells (APCs), such as dendritic cells and macrophages (Fig. 5*I*). CD169$^+$ macrophages are resident in lymph nodes and play a key role in immune regulation (27). This spatial colocalization suggests that APCs at the injection site internalize and transport the antigenic proteins to the iLNs, facilitating lymph node-resident immune activation (Fig. 5*J*).

Discussion

LNP-mediated delivery of mRNA has emerged as a cornerstone technology in nucleic acid vaccine development (3). Despite its clinical success, the mechanisms driving the immunogenicity of mRNA-LNP vaccines remain poorly understood (8, 28). In this study, we sought to elucidate the biodistribution patterns of both mRNA-expressed antigens and their LNP carriers, which is critical for understanding how immune activation is initiated. Through combined application of ^{19}F NMR and qPCR, we found that antigen expression was predominantly localized at the injection site, which subsequently recruited immune cells that migrated to the iLNs. These findings provide insights into the spatial dynamics of antigen presentation and immune activation

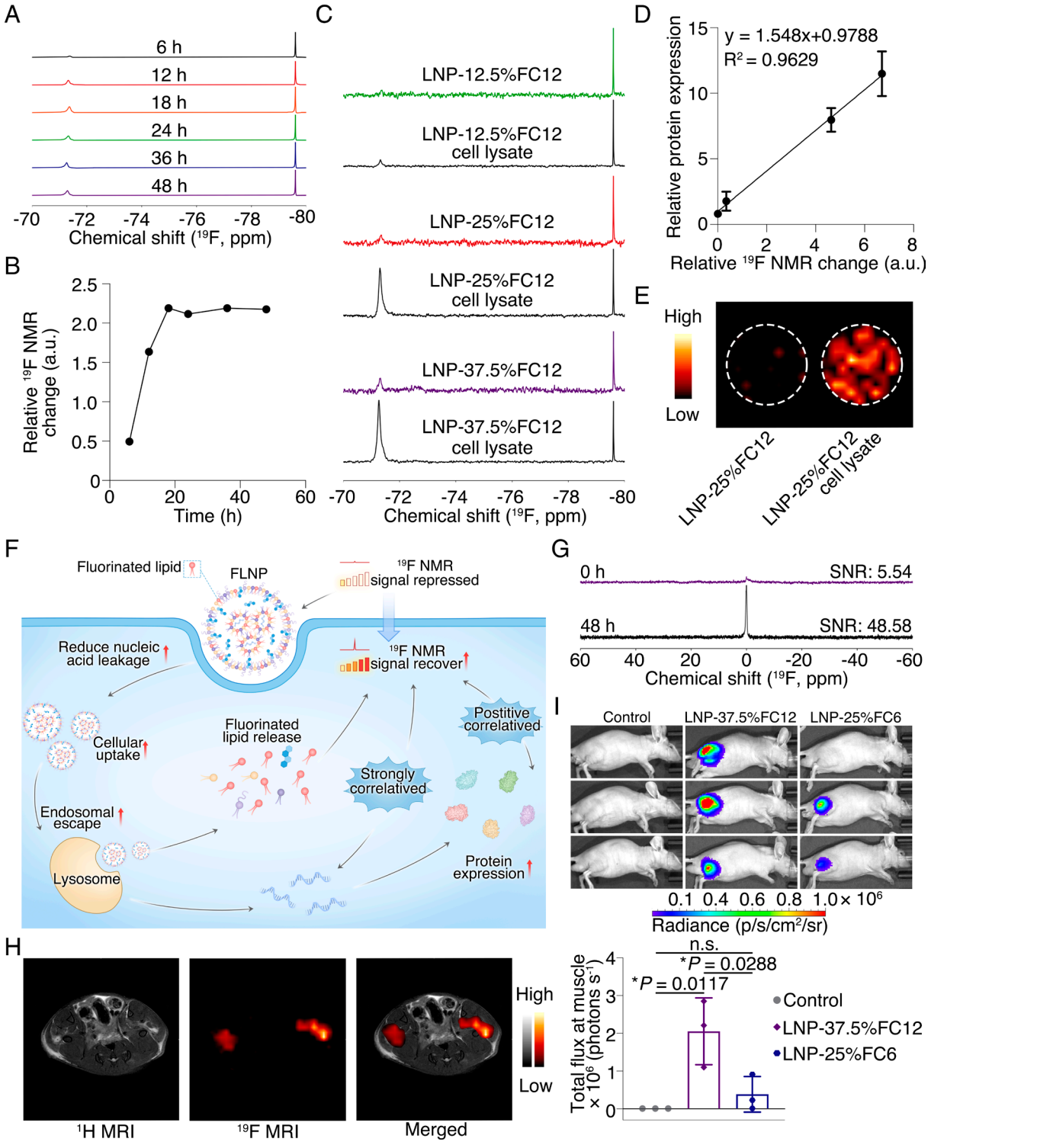

Fig. 4. Correlation between ^{19}F NMR signal recovery and nucleic acid release during FLNP transfection. (*A* and *B*) ^{19}F NMR and quantitative analysis of 293T cells treated with LNP-25%FC12 for 6 to 48 h. (*C*) ^{19}F NMR of LNP-12.5%FC12, LNP-25%FC12, or LNP-37.5%FC12 and 293T cells treated with corresponding FLNPs for 18 h. CF_3NaO_3S (−79.6 ppm) was used as the ^{19}F NMR reference at 1 mM. (*D*) Linear correlation between the change in ^{19}F NMR signal and EGFP intensity. (*E*) ^{19}F MRI of cell lysates. 293T cells were treated with LNP-25%FC12 for 48 h, then lysed with RIPA buffer. (*F*) Schematic representation of FLNPs enhancing nucleic acid delivery while simultaneously enabling noninvasive, real-time monitoring of nucleic acid release via ^{19}F NMR. (*G*) The ^{19}F NMR of LNP-37.5%FC12 (−71.3 ppm) and mice intramuscularly injected with LNP-37.5%FC12 for 48 h. (*H*) ^{1}H T_1-weighted/^{19}F dual-nuclei MRI of mice intramuscularly injected with LNP-37.5%FC12 for 48 h. (*I*) Representative in vivo bioluminescence images of mice treated with PBS, LNP-37.5%FC12, or LNP-25%FC6 for 24 h. In vivo bioluminescence imaging at 24 h posttreatment of mLuc-loaded LNPs (n = 3). Mice were *i.m.* injected with mLuc-loaded LNPs (5 μg mRNA per mouse) in the right gastrocnemius muscle.

following mRNA vaccination and support the rational design of future LNP formulations.

Previous studies have extensively validated that fluorination enhances the delivery efficiency of various gene vectors, including fluoropolymers (29), fluorinated dendrimers (30), and FLNPs (31, 32). These systems consistently showed transfection efficiencies comparable to commercial standards (e.g., Lipofectamine) and often exceeded their nonfluorinated analogs by twofold to threefold in

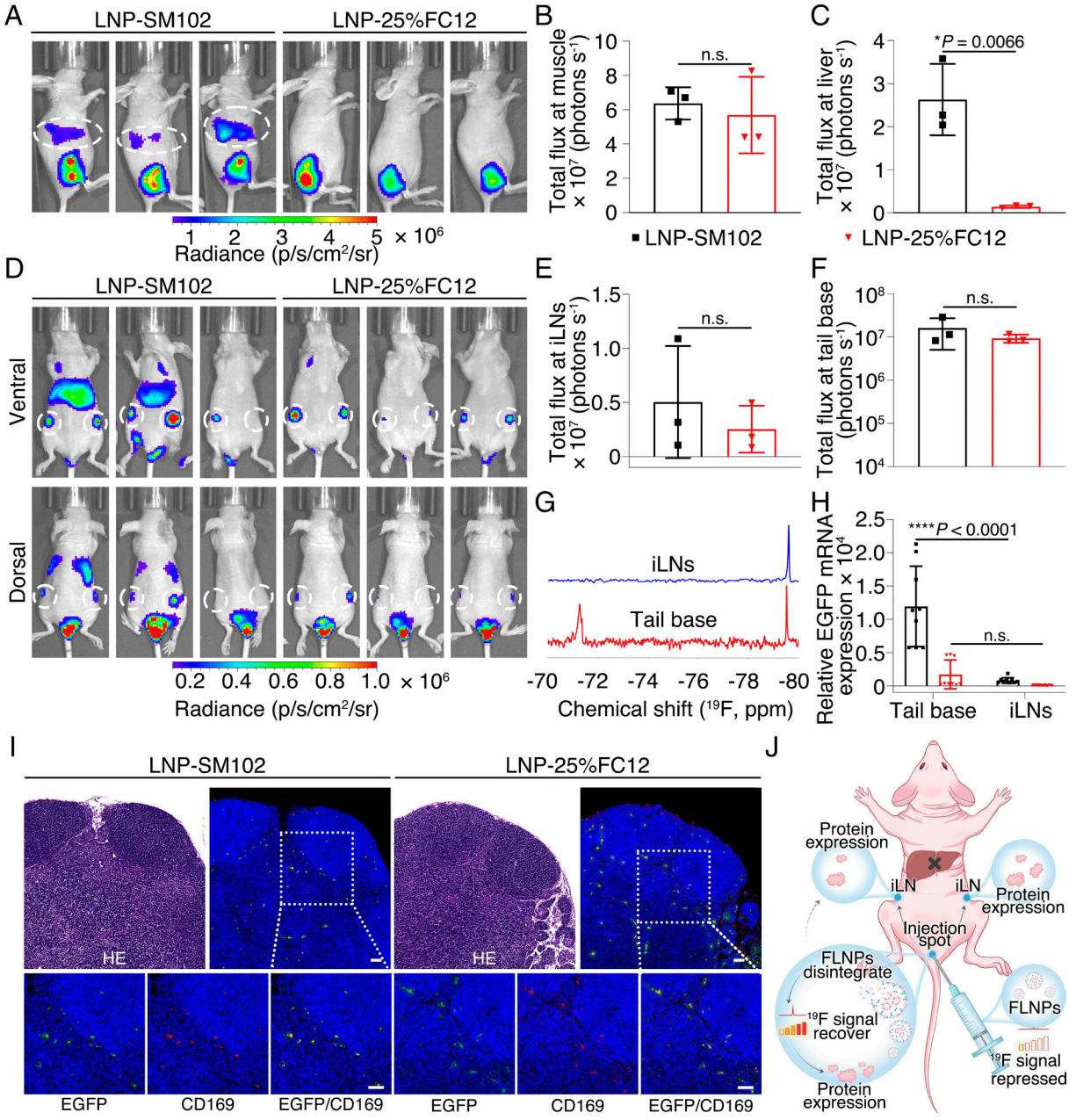

Fig. 5. ^{19}F NMR reveals FLNP-mediated delivery to iLNs for vaccine applications. (*A*) In vivo bioluminescence imaging at 24 h posttreatment of mLuc-loaded LNPs (n = 3). Mice were *i.m.* injected with mLuc-loaded LNPs (5 μg mRNA per mouse) at the right gastrocnemius muscle. Dashed circles indicate livers. Total flux at the injection site (*B*) and livers (*C*) were quantified. (*D*) In vivo bioluminescence imaging at 24 h posttreatment of mLuc-loaded LNPs (n = 3). Mice were *s.c.* injected with mLuc-loaded LNPs (5 μg mRNA per mouse) at the tail base. Dashed circles indicate iLNs. Total flux at the two iLNs (*E*) and injection site (*F*) was quantified. (*G*) ^{19}F NMR of tissue lysates from the iLNs or tail base after 24 h of treatment with LNP-25%FC12. CF_3NaO_3S (−79.6 ppm) at 1 mM was used as the reference. (*H*) EGFP mRNA expression in iLNs and tail base tissues, analyzed by RT-qPCR with GAPDH as reference gene. Tissues were collected 6 h postinjection of mEGFP-loaded LNPs (5 μg mRNA per mouse, n = 3). (*I*) Fluorescence microscopy of iLNs 24 h post–s.c. injection of mEGFP-loaded LNPs, showing EGFP expression (green), CD169$^+$ cells (red), and nuclei (DAPI, blue). (Scale bar, 50 μm.) (*J*) Schematic representation illustrating that changes in the ^{19}F NMR signal at the injection site and iLNs indicate antigen uptake by antigen-presenting cells, which then migrate to the iLNs.

cellular models (32). Our findings align well with these observations, further confirming the potential of fluorination to enhance gene delivery systems.

An ideal gene delivery vehicle should provide comprehensive protection for the payload across all delivery stages, encompassing extracellular targeting, endocytosis, and endosome escape before release into the cytoplasm (33, 34). Premature nucleic acid leakage during this process poses a significant risk of degradation by nuclease, ultimately compromising transfection inefficiency. While traditional optimization efforts for LNP formulations have primarily focused on enhancing cell uptake and endosome escape (31, 35), our study introduces a unique perspective: Fluorinated lipids provide comprehensive protection to nucleic acids at every stage of delivery, including the often-overlooked endocytosis phase, where transient exposure may occur. This added layer of protection contributes significantly to the superior transfection efficiency observed with FLNPs compared to conventional LNPs, emphasizing the importance of addressing the entire gene delivery pathway rather than focusing on isolated steps.

Furthermore, our results establish that recovery of ^{19}F NMR/MRI signals correlates with the disassembly of FLNPs and the intracellular release of nucleic acids. This correlation offers a noninvasive method to monitor nucleic acid release in real time and predict transfection outcomes. Notably, the applicability of this strategy may extend beyond nucleic acids to other cytosolic macromolecules,

such as peptides or proteins, suggesting broad utility for ^{19}F-labeled carriers in intracellular delivery applications.

To identify optimal formulations, we systematically screened FLNPs composed of various fluorinated lipids and doping ratios. We identified LNP-25%FC12 as a lead candidate that balances effective transfection with reduced off-target expression. However, several limitations should be acknowledged.

First, the observed enhancement in transfection efficiency may not be attributed solely to fluorination, as the fluorinated lipids used are not direct analogs of SM102. Although doping with fluorinated lipids largely preserves the structure integrity of the original LNPs, entirely fluorinated lipid-based LNPs may exhibit distinct structural properties, which merit further exploration.

Second, our assessment of endosomal escape relied on fluorescence colocalization (Cy5-LNP vs. LysoTracker), where noncolocalized red signals were interpreted as evidence of escape (34). Although straightforward, this method is indirect, resolution-limited, and susceptible to overestimation. More rigorous approaches, such as parallel electron microscopy, would allow more precise quantification (36).

Third, our primary in vivo screening was performed using pDNA rather than mRNA. Due to differences in molecular weight, structure, and packaging, pDNA may exhibit different interactions with fluorinated lipids than mRNA, potentially leading to more pronounced ^{19}F signal attenuation. Bridging the methodological gap between pDNA- and mRNA-based screening will require improved NMR/MRI hardware sensitivity and optimized labeling strategies to facilitate accurate monitoring of RNA-based formulations.

Finally, the current screening method is constrained by its low throughput, as overlapping fluorine chemical shifts preclude multiplexed evaluation of FLNP candidates. To address this limitation, we are developing fluorinated lipids with spectrally resolvable ^{19}F signatures, enabling simultaneous in vivo assessment of multiple FLNP variants. This innovation will significantly enhance the scalability and translational potential of our platform.

Materials and Methods

Materials. 1,2-Distearoyl-sn-glycero-3-phosphocholine (DSPC, ≥95%) and 1,2-dimyristoyl-rac-glycero-3-methoxypolyethylene glycol-2000 (DMG-PEG 2000, ≥90%) were purchased from Ruixi Biological Technology in Xi'an, China. Cholesterol (≥99%) was acquired from Sigma-Aldrich in Shanghai, China. Heptadecan-9-yl 8-((2-hydroxyethyl)(6-oxo-6-(undecyloxy)hexyl)amino)octanoate) (SM102, 98.7%) was obtained from Sinopeg in Xiamen, China. pEGFP and pLuc were purchased from Brain Case in Shenzhen, China. The mRNA encoding Enhanced Green Fluorescent Protein (mEGFP) or firefly luciferase (mLuc) were purchased from Absin, Shanghai, China. The nucleic acid labeling kit was sourced from Thermo Fisher in Waltham, USA. The 293T cell line was obtained from the cell bank of the Chinese Academy of Sciences in Shanghai, China.

General Information. ^{1}H, ^{13}C, ^{19}F NMR spectra were recorded using Bruker 400 MHz and 500 MHz instruments. Chemical shifts are reported in parts per million (ppm). ^{1}H NMR spectra were referenced to tetramethylsilane (d, 0.00 ppm) using $CDCl_3$ (s, 7.26 ppm) as the solvent, and ^{13}C NMR spectra were referenced to the solvent carbons (77.2 ppm for $CDCl_3$). ^{19}F NMR spectra were referenced to 2% sodium triflate (s, −79.6 ppm) in D_2O. High-resolution mass spectra (HRMS) were recorded using a Thermo Fisher Scientific Q Exactive Focus. The UV-vis absorption spectra were carried out by a Shimadzu UV-2 spectrophotometer (UV-vis spectrometer). The fluorescence spectra were measured on an Edinburgh FS5 fluorescence spectrometer equipped with a 150 W xenon lamp.

Synthesis of Cy5-Labeled Nucleic Acids. Tiangen High Pure Maxi Plasmid Kit (DP116) (Tiangen, China) was used to extract the plasmids expressing EGFP or Luciferase, which were then diluted to 1 μg/μL for subsequent experiments. Plasmids were labeled Cy5 by using Ulysis™ Alexa Fluor™ 647 Nucleic Acid Labeling Kit from Thermo Fisher in the United States following the manufacturer's instructions. The pEGFP-Cy5 were then purified from the excess labeling reagent using a 3 kDa molecular weight cut-off cassette and stored at −20 °C.

Synthesis of Cy3-Labeled Fluorinated Lipids. Fluorinated lipids (FC12 and FC6) were first reacted with 4-bromo-1-butyne in acetonitrile with potassium carbonate and potassium iodide to generate alkyne-labeled derivatives. These intermediates then underwent a copper-catalyzed click reaction with Cy3-N_3, yielding Cy3-labeled fluorinated lipids (Cy3-FC12 and Cy3-FC6). Using the same strategy, Cy3-labeled SM102 (Cy3-SM102) was synthesized. Alkyne-labeled SM102 was efficiently prepared by Williamson ether synthesis between SM102 and 4-bromo-1-butyne, followed by click conjugation with Cy3-N_3. Full details of the synthesis procedures are provided in the *SI Appendix*.

LNP Formulation and Characterization. Ionizable lipids (with or without fluorinated lipids), DSPC, cholesterol, and DMG-PEG2000 at a designated molar ratio were dissolved in the ethanol phase. Nucleic acids were dissolved in 50 mM citrate buffer (pH = 3.0). For initial in vitro screening, LNPs were prepared by pipette mixing the aqueous and ethanol phases at a 3:1 volume ratio, followed by dilution in 1× PBS for cell treatment (37). For subsequent experiments, LNPs were formulated by microfluidic mixing (38, 39). The aqueous phase and ethanol phase were mixed at a 3:1 volume ratio using a commercial double-sided herringbone microstructure chip (Model SHM DS; NanoMicroFlo Technology Co., Ltd.), with a channel width of 300 μm, depth of 200 μm, mixing length of 90 mm, and a flow rate of 4 mL/min. Detailed fabrication specifications and operating protocols are available from the manufacturer (https://www.nanomicroflo.com/).

Cy3- or Cy5-labeled LNPs were obtained by tagging the fluorinated lipid or pDNA prior to mixing the ethanol phase and aqueous phase. Impurities were removed from LNP crude solutions using PD-10 column chromatography. The LNPs were then dialyzed against 1× PBS using a 100 kDa molecular weight cut-off cassette and then stored at 4 °C.

The pDNA encapsulation efficiency of LNPs was evaluated by calculating the ratio of Cy5 signal in the eluent (unencapsulated pDNA) to the total Cy5 signal added using fluorescence spectrometer. The encapsulation efficiency of mRNA within the LNPs was quantified using the Quant-iT RiboGreen RNA assay kit (Thermo Fisher, USA). To distinguish between encapsulated and free mRNA, each LNP formulation was diluted 20-fold in two different solutions: a standard 1× TE buffer and a 1× TE buffer containing 0.1% Triton X-100 (Solarbio, China), which disrupts the lipid shells to release the RNA. The diluted samples, alongside an RNA standard curve, were added into a black, clear-bottom 96-well plate. After adding 100 μL of RiboGreen reagent to each well, fluorescence was measured at an emission wavelength of 520 nm using a microplate reader (Molecular Devices, UK). The RNA concentration for each sample condition was determined by interpolating values from the standard curve, which was generated by univariate least-squares linear regression. Encapsulation efficiency (EE) was then calculated using the formula: EE (%) = (X − Y)/X × 100, where X represents the total RNA content (measured in Triton X-100) and Y represents the unencapsulated, free RNA content (measured in TE buffer alone).

The size distribution, PDI, and ζ-potential of nanoparticles were determined by a DLS instrument (Malvern, Nano ZS 90, UK). The hydrodynamic diameter was derived from the diffusion coefficient (D), which was obtained by fitting the correlation curve to an exponential model. The diameter was then calculated using the Stokes–Einstein equation ($D_H = kT/3\pi\eta D$), where k is the Boltzmann constant, T is the absolute temperature, and η is the solvent viscosity. The number-weighted mean diameters reported in the manuscript were determined from the size distribution using Mie theory conversion.

The apparent pKa, defined as the pH at which 50% of the ionizable groups in the LNP are protonated, was determined using a 6-(*p*-toluidinyl)naphthalene-2-sulfonic acid (TNS) fluorescence assay. Buffered solutions containing 150 mM sodium chloride, 20 mM sodium phosphate, 20 mM citrate, and 20 mM Tris-HCl were prepared and adjusted to pH values ranging from 3.0 to 12.0. For each measurement, 193 μL of the pH-adjusted buffer and 5 μL of the LNP formulation were dispensed in quadruplicate into black 96-well plates. Subsequently, 2 μL of TNS was added to each well to a final concentration of 6 μM. Fluorescence intensity was recorded using a microplate reader (Molecular Devices, UK) with excitation at 322 nm and emission at 431 nm.

Cryo-TEM imaging was performed using a Thermo Scientific™ Glacios™ transmission electron microscope. Samples were blotted for 3 s with a blot force of 3, followed by a wait time of 3 s before vitrification.

Stability Test of LNPs. The LNPs were diluted with 1× PBS, and nucleic acids were dissolved in ddH_2O. Both solutions were mixed with or without DNase I and

incubated at 37 °C for 10 min. The final concentration of nucleic acids in each sample was 0.1 μg/μL. The stability of LNPs was analyzed using electrophoretic mobility-shift assays in a 1% agarose gel in standard TAE buffer for 1 h. The nucleic acid bands were detected using the iBright FL 1500 Imaging System from Thermo Fisher in the United States. Naked pDNA served as a control.

Cell Culture and Transfection of LNP. 293T cells were cultured in DMEM supplemented with 10% FBS and 1% penicillin–streptomycin and incubated at 37 °C in a 5% CO_2 environment. To evaluate mRNA delivery efficiency in vitro, 2×10^4 293T cells were seeded in 35 mm glass-bottom dishes from NEST, China. After overnight incubation at 37 °C, LNPs containing 390 ng of pDNA or 400 ng of mRNA were added to each dish. The cells were then incubated for 48 or 24 h, respectively, at 37 °C. After incubation, cells were stained with DAPI, and EGFP expression was assessed using a CLSM. The commercial transfection reagent Lipo8000 from Beyotime, China, was used as a positive control for pDNA-loaded LNPs.

Cytotoxicity Studies. 293T cells were incubated with LNPs for 48 h. The cell viability was measured using the cell counting kit-8 (CCK-8) assay according to the manufacturer's instructions (APExBIO. USA). The results were measured using a microplate reader at 450 nm.

Imaging with Confocal FRET Microscopy. Images were captured using a Nikon A1R/A1 CLSM from Nikon, Japan. The filter sets used were as follows: the green channel (donor Cy3: excitation/donor emission = 561/570 nm), the red channel (acceptor Cy5: excitation/acceptor emission = 640/670 nm), and the FRET channel (FRET: donor excitation/acceptor emission = 561/670 nm). Three different types of samples, containing only donor, only acceptor, and both donor and acceptor, were examined using each of the three filters (40).

Cell Uptake of LNPs. 293T cells were seeded at 5×10^4 cells/well in a 12-well plate 1 d before transfection. The cells were then incubated with Cy5-labeled LNPs for 1, 2, 4, 6, 8, and 12 h. Subsequently, the cells were analyzed using flow cytometry (Beckman Coulter). Each assay was performed in triplicate.

In Vitro mLuc Delivery. 293T cells were seeded onto a 96-well plate at a density of 12,500 per well and incubated overnight. Cells were then treated with pLuc-loaded LNPs for 48 h or with mLuc-loaded LNPs for 24 h. Luciferase expression was evaluated by Luciferase Reporter 1000 Assay System (E4550, Promega) according to the manufacturer's protocols. The relative luciferase expression was reported as relative light units normalized to cell number. Free pDNA or mRNA served as controls.

Endosomal Escape of LNPs. 293T cells were seeded at 2×10^5 cells in 35 mm glass-bottom dishes 1 d before transfection. The cells were then incubated with Cy5-labeled LNPs for 2 to 4 h. Afterward, the cells were sequentially stained with LysoTracker Green (Beyotime, China) for 30 min and Hoechst 33342, also from Beyotime, for another 30 min. Images were captured immediately using a confocal laser scanning microscope.

^{19}F NMR Measurements. All ^{19}F NMR experiments utilized CF_3NaO_3S as an internal standard to determine the fluorine content. Briefly, the mixture of fluorinated lipid and CF_3NaO_3S was placed in an NMR tube, and one-dimensional (1D) ^{19}F spectra were acquired using the following parameters: Prescan delay = 18 μs, Transmitter frequency offset = −35,487.01 Hz, Number of scans = 128, Receiver gain = 32. The ^{19}F NMR spectra exhibited two narrow peaks, corresponding to the fluorinated lipid and CF_3NaO_3S, respectively.

Cell Experiment for ^{19}F NMR/MRI. After transfecting 293T cells with pEGFP loaded LNP-25%FC12 for 6, 12, 18, 24, 36, and 48 h, 1×10^8 cells were harvested and lysed using RIPA buffer. The cell lysates were then centrifuged at 12,000 g for 5 min. The supernatant solutions were then collected for ^{19}F NMR/MRI assessment.

Animal. All experimental procedures involving animals strictly adhered to the Guideline for Animal Care and Use, Innovation Academy for Precision Measurement Science and Technology, Chinese Academy of Sciences (APM21013T). The mouse experimental protocols were conducted in accordance with the Regulations for the Administration of Affairs Concerning Experimental Animals, which were approved by the State Council of the People's Republic of China. BALB/c female nude mice and C57BL/6 female mice (6 to 8 wk old, approximately 20 g) were obtained from Beijing Vital River Laboratory Animal Technology Co. Ltd. The mice were fed a standard irradiated rodent chow diet at the same time every day and housed in a room with a 12-h light–dark cycle at 22 °C, with lights off from 6 p.m. to 6 a.m.

In Vivo ^{19}F MRI. The mice received 50 μL of pDNA-loaded FLNPs in each gastrocnemius muscle, respectively. 48 h after injection, the mice were anesthetized with an intraperitoneal injection of 150 μL of 1% sodium pentobarbital solution. ^{1}H/^{19}F MRI was performed using a 9.4T wide-bore NMR spectrometer. Radio frequency transmission and reception were facilitated using 30 mm inner diameter ^{1}H (400 MHz) and ^{19}F (376.5 MHz) coils.

^{1}H MRI was carried out using the rapid acquisition with refocused echoes (RARE) method, with the following parameters: number of averages = 4, repetition time (TR) = 6,000 ms, effective time (TE) = 56 ms, field of view (FOV) = 30 mm × 30 mm, slice thickness (ST) = 1 mm, and matrix size = 256 × 256.

For ^{19}F MRI, the parameters were number of averages = 256, TR = 200 ms, TE = 3 ms, matrix size = 64 × 64, FOV = 30 mm × 30 mm, ST = 14.82 mm, rare factor = 4, and bandwidth = 2,000 Hz. All raw data were processed using MATLAB (R2022a, MathWorks, Natick, MA).

Transfection of LNPs In Vivo. Mice were injected with mRNA-loaded LNPs (5 μg mRNA per mouse) at the right gastrocnemius muscle or tail base. At 24 h postinjection, mice were intraperitoneally (*i.p.*) injected with d-luciferin potassium salt [150 mg/kg (body weight)], and bioluminescence imaging was performed on an IVIS imaging system (PerkinElmer). Regions of interest were quantified as the average radiance (photons/s/cm^2/sr) using Living Image software.

^{19}F NMR Analysis of Mouse Tissue. Mouse tissues, including gastrocnemius muscle, iLNs, and tail base, were collected 24 h after treatment with mRNA-loaded LNPs, or 48 h after treatment with pDNA-loaded LNPs. The tissues were lysed in RIPA buffer and centrifuged at 12,000× g for 5 min. The resulting supernatant was collected for ^{19}F NMR analysis.

RNA Isolation and Real–Time qPCR Analysis. Total RNA was isolated from frozen tissues using TRIzol reagent (Thermo Fisher, Waltham, MA, USA) following the manufacturer's instructions. The RNA's purity and concentration were measured with a NanoDrop Ultra Spectrophotometer (NanoDrop Technologies, Wilmington, USA). Next, 1 μg of the RNA was reverse transcribed, and RT-qPCR was conducted using a SYBR Green mix (YEASEN, China) on a StepOnePlus™ Real-Time PCR System (Thermo Fisher Scientific, USA) in a 96-well format. GAPDH was used as the reference gene for normalization, and relative EGFP expression levels were determined using the 2−^ΔΔCT method. The primer sequences were as follows: GAPDH: Forward: 5′-CATCACTGCCACCCAGAAGACTG-3′; Reverse: 5′-ATGCCAGTGAGCTTCCCGTTCAG-3′. EGFP: Forward: 5′- AAGCAGAAGAACGGCATCA-3′; Reverse: 5′- GGCGGTCACGAACTCCA-3′.

Statistical Analysis. In vitro experiments were conducted in triplicates to ensure high statistical power. Statistical differences between and among groups were assessed using Student's *t* test and ANOVA followed by Tukey's post hoc tests, respectively. GraphPad Prism 10 software was utilized for statistical analyses, and a significance level of $P < 0.05$ was set as the threshold for determining statistical significance.

Data, Materials, and Software Availability. Study data are included in the article and/or *SI Appendix*.

ACKNOWLEDGMENTS. This work was supported by the National Natural Science Foundation of China (22374157 and 82127802); Strategic Priority Research Program, CAS (XDB0540000 and XDC0170000); Key Research Program of Frontier Sciences, CAS (ZDBS-LY-JSC004); and Major Program (JD) of Hubei Province (2023BAA021).

Author affiliations: [a]State Key Laboratory of Magnetic Resonance Spectroscopy and Imaging, National Center for Magnetic Resonance in Wuhan, Wuhan Institute of Physics and Mathematics, Innovation Academy for Precision Measurement Science and Technology, Chinese Academy of Sciences–Wuhan National Laboratory for Optoelectronics, Huazhong University of Science and Technology, Wuhan 430071, China; [b]University of Chinese Academy of Sciences, Beijing 100049, China; [c]Key Laboratory of Biomedical Engineering of Hainan Province, School of Biomedical Engineering, Hainan University, Haikou 570228, China; and [d]Department of Neurosurgery and Medicine Institute for Neuroscience Discovery, University of Maryland School of Medicine, Baltimore, MD 21201

1. N. Chaudhary, D. Weissman, K. A. Whitehead, mRNA vaccines for infectious diseases: Principles, delivery and clinical translation. *Nat. Rev. Drug Discov.* **20**, 817–838 (2021).
2. N. Pardi, M. J. Hogan, F. W. Porter, D. Weissman, mRNA vaccines–A new era in vaccinology. *Nat. Rev. Drug Discov.* **17**, 261–279 (2018).
3. P. Polack Fernando *et al.*, Safety and efficacy of the BNT162b2 mRNA covid-19 vaccine. *N. Engl. J. Med.* **383**, 2603–2615 (2020).
4. X. Hou, T. Zaks, R. Langer, Y. Dong, Lipid nanoparticles for mRNA delivery. *Nat. Rev. Mater.* **6**, 1078–1094 (2021).
5. L. Xue *et al.*, High-throughput barcoding of nanoparticles identifies cationic, degradable lipid-like materials for mRNA delivery to the lungs in female preclinical models. *Nat. Commun.* **15**, 1884 (2024).
6. D. Loughrey, J. E. Dahlman, Non-liver mRNA delivery. *Acc. Chem. Res.* **55**, 13–23 (2022).
7. S. A. Dilliard, D. J. Siegwart, Passive, active and endogenous organ-targeted lipid and polymer nanoparticles for delivery of genetic drugs. *Nat. Rev. Mater.* **8**, 282–300 (2023).
8. M. Buckley *et al.*, Visualizing lipid nanoparticle trafficking for mRNA vaccine delivery in non-human primates. *Mol. Ther.* **33**, 1105–1117 (2024).
9. A. Aung *et al.*, Low protease activity in B cell follicles promotes retention of intact antigens after immunization. *Science* **379**, eabn8934 (2023).
10. B. J. Read *et al.*, Mannose-binding lectin and complement mediate follicular localization and enhanced immunogenicity of diverse protein nanoparticle immunogens. *Cell Rep.* **38**, 1–15 (2022).
11. Y. Suzuki *et al.*, Design and lyophilization of lipid nanoparticles for mRNA vaccine and its robust immune response in mice and nonhuman primates. *Mol. Ther. Nucleic Acids* **30**, 226–240 (2022).
12. K. E. Lindsay *et al.*, Visualization of early events in mRNA vaccine delivery in non-human primates via PET–CT and near-infrared imaging. *Nat. Biomed. Eng.* **3**, 371–380 (2019).
13. A. Cagigi, K. Loré, Immune responses induced by mRNA vaccination in mice. Monkeys and humans. *Vaccines* **9**, 1–14 (2021).
14. S. Ols *et al.*, Route of vaccine administration alters antigen trafficking but not innate or adaptive immunity. *Cell Rep.* **30**, 3964–3971 (2020).
15. F. Liang *et al.*, Efficient targeting and activation of antigen-presenting cells *in vivo* after modified mRNA vaccine administration in rhesus macaques. *Mol. Ther.* **25**, 2635–2647 (2017).
16. J. Xu *et al.*, A general strategy towards personalized nanovaccines based on fluoropolymers for post-surgical cancer immunotherapy. *Nat. Nanotechnol.* **15**, 1043–1052 (2020).
17. Y. Zhao *et al.*, Nanomechanical action opens endo-lysosomal compartments. *Nat. Commun.* **14**, 6645 (2023).
18. C. L. Ge *et al.*, Fluorinated α-helical polypeptides synchronize mucus permeation and cell penetration toward highly efficient pulmonary siRNA delivery against acute lung injury. *Nano Lett.* **20**, 1738–1746 (2020).
19. J. Ruiz-Cabello, B. P. Barnett, P. A. Bottomley, J. W. Bulte, Fluorine (^{19}F) MRS and MRI in biomedicine. *NMR Biomed.* **24**, 114–129 (2011).
20. L. Wu *et al.*, Perfluorocarbons-based ^{19}F magnetic resonance imaging in biomedicine. *Int. J. Nanomed.* **15**, 7377–7395 (2020).
21. H. W. M. van Laarhoven, D. W. J. Klomp, Y. J. L. Kamm, C. J. A. Punt, A. Heerschap, In vivo monitoring of capecitabine metabolism in human liver by ^{19}fluorine magnetic resonance spectroscopy at 1.5 and 3 tesla field strength. *Cancer Res.* **63**, 7609–7612 (2003).
22. L. R. Baden *et al.*, Efficacy and safety of the mRNA-1273 SARS-CoV-2 vaccine. *N. Engl. J. Med.* **384**, 403–416 (2021).
23. M. A. Liu, A comparison of plasmid DNA and mRNA as vaccine technologies. *Vaccines* **7**, 37 (2019).
24. Y. Werle, M. Kovermann, Fluorine labeling and 19F NMR spectroscopy to study biological molecules and molecular complexes. *Chem. Eur. J.* **31**, e202402820 (2025).
25. Y. Li *et al.*, Probing rotaxane dynamics with ^{19}F NMR/MRI: Unveiling the roles of mechanical bond and steric hindrance. *Anal. Chim. Acta* **1319**, 342983 (2024).
26. S. Stoffel, Q. W. Zhang, D. H. Li, B. D. Smith, J. W. Peng, NMR relaxation dispersion reveals macrocycle breathing dynamics in a cyclodextrin-based rotaxane. *J. Am. Chem. Soc.* **142**, 7413–7424 (2020).
27. L. Chávez-Galán, M. L. Olleros, D. Vesin, I. Garcia, Much more than M1 and M2 macrophages, there are also CD169$^+$ and TCR$^+$ macrophages. *Front. Immunol.* **6**, 263 (2015).
28. K. J. Hassett *et al.*, mRNA vaccine trafficking and resulting protein expression after intramuscular administration. *Mol. Ther. Nucleic Acids* **35**, 102083 (2024).
29. E. Tan *et al.*, Statistical versus block fluoropolymers in gene delivery. *J. Mater. Chem. B* **6**, 7230–7238 (2018).
30. M. Wang, H. Liu, L. Li, Y. Cheng, A fluorinated dendrimer achieves excellent gene transfection efficacy at extremely low nitrogen to phosphorus ratios. *Nat. Commun.* **5**, 3053 (2014).
31. H. P. Zhang *et al.*, Fluorinated lipid nanoparticles for enhancing mRNA delivery efficiency. *ACS Nano* **18**, 7825–7836 (2024).
32. H. A. Huo *et al.*, A fluorinated ionizable lipid improves the mRNA delivery efficiency of lipid nanoparticles. *J. Mater. Chem. B* **11**, 4171–4180 (2023).
33. K. Lam *et al.*, Optimizing lipid nanoparticles for delivery in primates. *Adv. Mater.* **35**, e2211420 (2023).
34. X. Han *et al.*, Adjuvant lipidoid-substituted lipid nanoparticles augment the immunogenicity of SARS-CoV-2 mRNA vaccines. *Nat. Nanotechnol.* **18**, 1105–1114 (2023).
35. J. Lv, H. Wang, G. Rong, Y. Cheng, Fluorination promotes the cytosolic delivery of genes, proteins, and peptides. *Acc. Chem. Res.* **55**, 722–733 (2022).
36. J. Gilleron *et al.*, Image-based analysis of lipid nanoparticle-mediated siRNA delivery, intracellular trafficking and endosomal escape. *Nat. Biotechnol.* **31**, 638–646 (2013).
37. X. Han *et al.*, In situ combinatorial synthesis of degradable branched lipidoids for systemic delivery of mRNA therapeutics and gene editors. *Nat. Commun.* **15**, 1762 (2024).
38. M. M. Billingsley *et al.*, Ionizable lipid nanoparticle-mediated mRNA delivery for human CAR T cell engineering. *Nano Lett.* **20**, 1578–1589 (2020).
39. C. Mo *et al.*, SARS-CoV-2 mRNA vaccine requires signal peptide to induce antibody responses. *Vaccine* **41**, 6863–6869 (2023).
40. A. M. Blanco, L. Rausell, B. Aguado, M. Perez-Alonso, R. Artero, A FRET-based assay for characterization of alternative splicing events using peptide nucleic acid fluorescence in situ hybridization. *Nucleic Acids Res.* **37**, e116 (2009).